

# Conductive single-phase SrMoO<sub>3</sub> epitaxial films synthesized in pure Ar ambience via plasma-assisted radio frequency sputtering

Mouli Roy-Chowdhury<sup>1</sup>, Cong He<sup>2</sup>, Ke Tang<sup>1,3</sup>, Hiroki Koizumi<sup>1,4</sup>, Zhenchao Wen<sup>1</sup>, Subhash Thota<sup>2</sup>, Hiroaki Sukegawa<sup>1</sup>, Tadakatsu Ohkubo<sup>1</sup> and Seiji Mitani<sup>1,3</sup>

<sup>1</sup>Center for Magnetic and Spintronic Materials, National Institute for Materials Science (NIMS), Tsukuba, Japan;

<sup>2</sup>Department of Physics, Indian Institute of Technology Guwahati, Guwahati, India;

<sup>3</sup>Graduate School of Science and Technology, University of Tsukuba, Tsukuba, Japan;

<sup>4</sup>Center for Science and Innovation in Spintronics (CSIS), Tohoku University, Sendai, Japan

## ABSTRACT

The cubic perovskite SrMoO<sub>3</sub> with a paramagnetic ground state and remarkably low room-temperature resistivity has been considered as a suitable candidate for the new-era oxide-based technology. However, the difficulty of preparing single-phase SrMoO<sub>3</sub> thin films by hydrogen-free sputtering has hindered their practical use, especially due to the formation of thermodynamically favorable SrMoO<sub>4</sub> impurity. In this work, we developed a radio frequency sputtering technology enabling the reduction reaction and achieved conductive epitaxial SrMoO<sub>3</sub> films with pure phase from a SrMoO<sub>4</sub> target in a hydrogen-free, pure argon environment. We demonstrated the significance of controlling the target-to-substrate distance (TSD) on the synthesis of SrMoO<sub>3</sub>; the film resistivity drastically changes from 1.46 × 10<sup>5</sup> μΩ-cm to 250 μΩ-cm by adjusting the TSD. Cross-sectional microstructural analyses demonstrated that films with the lowest resistivity, deposited for TSD = 2.5 cm, possess a single-phase SrMoO<sub>3</sub> with an epitaxial perovskite structure. The formation mechanism of the conductive single-phase SrMoO<sub>3</sub> films can be attributed to the plasma-assisted growth process by tuning the TSD. Temperature-dependent resistivity and Hall effect studies revealed metal-like conducting properties for low-resistive SrMoO<sub>3</sub> films, while the high-resistive ones displayed semiconductor-like behavior. Our approach makes hydrogen-free, reliable and cost-efficient scalable deposition of SrMoO<sub>3</sub> films possible, which may open up promising prospects for a wide range of future applications of oxide materials.

## ARTICLE HISTORY

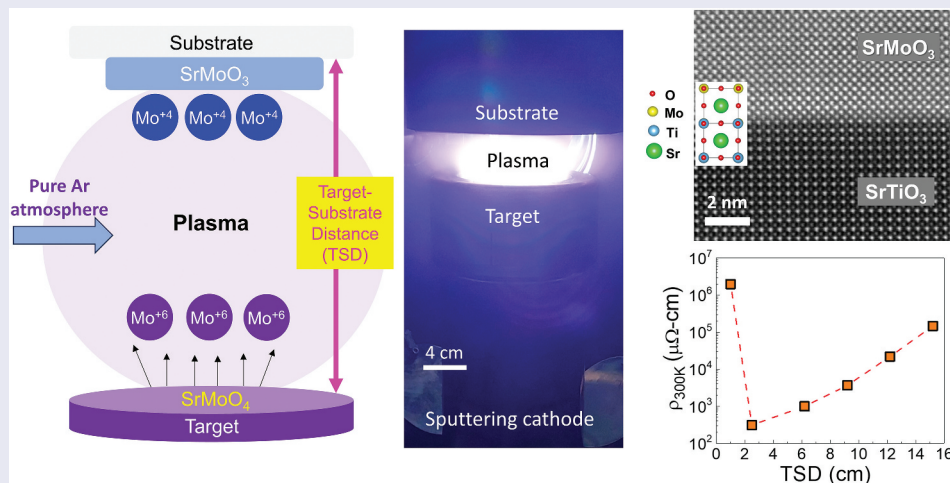
Received 3 May 2024

Revised 2 July 2024

Accepted 7 July 2024



## KEYWORDS


Conductive SrMoO<sub>3</sub>; epitaxial thin films; plasma-assisted sputtering; target-to-substrate distance



## IMPACT STATEMENT

For the first time, we developed a plasma-assisted RF sputtering technology enabling the reduction reaction for the synthesis of single-phase conductive SrMoO<sub>3</sub> epitaxial films from insulating SrMoO<sub>4</sub> in pure-argon atmosphere.

**CONTACT** Zhenchao Wen  [WEN.Zhenchao@nims.go.jp](mailto:WEN.Zhenchao@nims.go.jp)  Center for Magnetic and Spintronic Materials, National Institute for Materials Science (NIMS), 1-2-1 Sengen, Tsukuba 305-0047, Japan

 Supplemental data for this article can be accessed online at <https://doi.org/10.1080/14686996.2024.2378684>

© 2024 The Author(s). Published by National Institute for Materials Science in partnership with Taylor & Francis Group.

This is an Open Access article distributed under the terms of the Creative Commons Attribution-NonCommercial License (<http://creativecommons.org/licenses/by-nc/4.0/>), which permits unrestricted non-commercial use, distribution, and reproduction in any medium, provided the original work is properly cited. The terms on which this article has been published allow the posting of the Accepted Manuscript in a repository by the author(s) or with their consent.

## Introduction

Transition-metal oxides (TMOs) with the perovskite structure ( $ABO_3$ ) provide an excellent platform for exploring exceptional transport properties arising from the interplay of charge, spin, orbital, and lattice degrees of freedom [1–7]. The ongoing explosion of interest in TMO has led to an era of revolutionary inter-disciplinary research in spintronics, magnonics, and nano-engineering technology [8–11]. While the  $3d$  TMO received more attention than their  $4d$  and  $5d$  counterparts due to strong on-site Coulomb repulsion among the  $3d$  electrons and ease of synthesis [1–7,12], recent studies on heavy metal based  $4d$  TMOs like Ru and Ir oxides have been undertaken [8–11,13]. The  $4d$  TMO systems are characterized by extended  $d$  orbitals leading to strong neighboring orbital hybridization, weak on-site Coulomb repulsion energy, high charge-transfer and crystal-field splitting energies [14]. Pioneering studies on these systems have reported substantial spin-orbit coupling, large spin-Hall efficiency, high conductivity, and large carrier density, making them potential candidates for oxide-based electronic devices [15–22]. Among  $4d$  TMO compounds,  $SrMoO_3$  (SMO) has a cubic ( $Pm\bar{3}m$ ) perovskite structure and behaves as a Pauli paramagnetic band metal [14,15,17,23–26]. The  $4d-t_{2g}$  orbital of tetravalent Mo cations in SMO consists of two unpaired electrons responsible for the  $n$ -type conduction mechanism [27]. A low resistivity of  $5.1 \mu\Omega\cdot\text{cm}$  at room temperature (RT) was reported in its bulk form [23]. In view of its unique properties, SMO is one of the attractive candidates for applications in transparent conductors, microwave devices, and spintronic devices [15,17,28,29].

Nevertheless, the synthesis of monophasic SMO thin films remains a formidable challenge due to the formation of  $SrMoO_4$  ( $I4_1/a$ ) as a secondary phase. The high conductivity of the SMO films is susceptible to the stabilization of the thermodynamically unfavorable  $Mo^{4+}$  state ( $4d^2$  valence configuration) near the Fermi level [28]. It is particularly important to efficiently develop the synthesis parameters to be free of impurities in order to increase the conductivity of SMO films and to promote their widespread applications. Available reports on SMO indicate pulsed laser deposition (PLD) technique as its most popular synthesis method [24,26,27,30]. However, certain shortcomings such as restricted deposition area, particulate formation and high synthesis cost make PLD unsuitable for large-scale production. Radio frequency (RF) magnetron sputtering proves to be more effective as it enables uniform growth over large deposition substrates and has a high reproducibility rate [31–33]. Previous reports on the preparation of sputter-deposited SMO films have shown that  $H_2$ -Ar gas mixture is essential for single-phase SMO

synthesis [25,34,35]. However, the use of the  $H_2$  gas limits efficient scalable deposition for practical applications. Therefore, the development of an alternative sputtering technique that ensures the feasibility of low-cost,  $H_2$ -free, large-scale SMO deposition is strongly desirable.

In this study, we developed an RF sputtering technique to fabricate conductive single-phase SMO epitaxial thin films using an insulating  $SrMoO_4$  ceramic target in pure Ar ambience. The use of a small target-to-substrate distance (TSD) of 2.5 cm, where the substrate is directly exposed to the RF plasma of the  $SrMoO_4$  target, successfully yielded single-phase SMO(001) with resistivity down to  $250 \mu\Omega\cdot\text{cm}$  at RT via plasma assistance. Temperature dependence of the film resistivity and ordinary Hall effect revealed that the prepared low resistive SMO films exhibited metallic behavior characterized by high carrier concentration and moderate mobility.

## Experimental methodology

SMO thin films ( $\sim 30$  nm) were deposited on  $SrTiO_3$  (STO)(001) substrates using an ultrahigh vacuum RF magnetron sputtering chamber with a rotating-substrate configuration at a base pressure of  $1 \times 10^{-7}$  Pa. The STO substrates were pre-baked at  $800^\circ\text{C}$  for 1 h in a muffle furnace to ensure a flat surface before SMO deposition. A schematic illustration of the sputtering chamber is shown in Figure 1(a). A real-time image of the plasma emitted from a 3-inch-diameter  $SrMoO_4$  sintered target (Toshiba Manufacturing Co. Ltd, Japan) is shown in Figure 1(b). Pure Ar gas was used as the process gas for deposition. We investigated the sputtering parameters, including the input RF power, Ar pressure, substrate temperature, and TSD. The Sr:Mo atomic ratio in the thin films was confirmed using x-ray fluorescence technique (Rigaku Corporation, Japan; Model: ZSX Primus II). The crystal structures of the SMO films were characterized by *in-situ* reflection high energy electron diffraction (RHEED, manufactured by R-DEC Co. Ltd, Japan) and by *ex-situ* x-ray diffraction (XRD) techniques. Out-of-plane and in-plane XRD scans were performed on a SmartLab diffractometer from Rigaku Corporation, Japan, with  $Cu-K_{\alpha 1}$  radiation and an incident  $Ge(220)$  monochromator. Atomic force microscopy (AFM) technique was used to probe the surface morphology and roughness by employing a scanning probe microscope manufactured originally by Seiko Instruments Inc., Japan. Cross-sectional microstructural analysis was performed using scanning transmission electron microscopy (STEM), with specimens prepared through a standard lift-out method utilizing focus ion beam (FIB) on a FEI Helios5UX scanning electron microscope (SEM); high-angle annular dark-field STEM (HAADF-

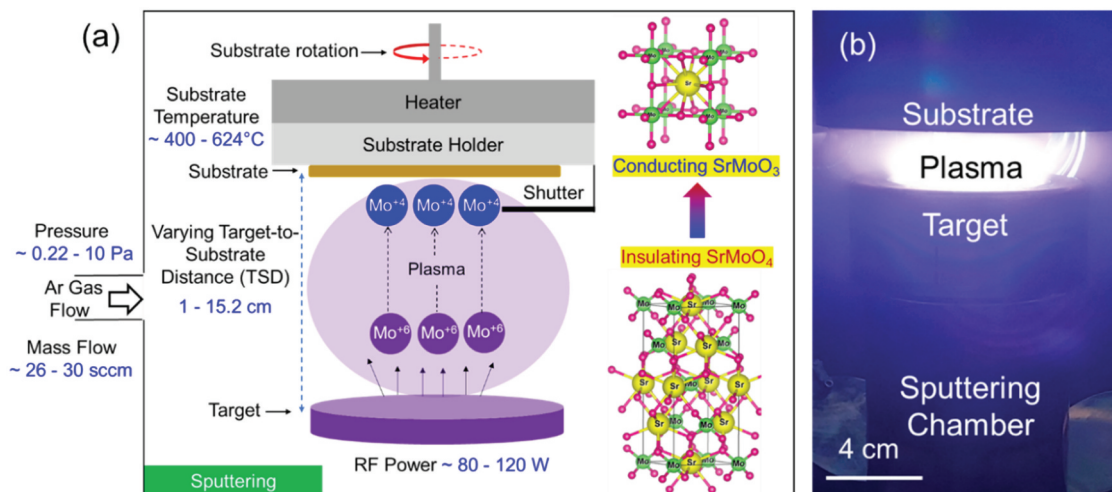


**Figure 1.** (a) A schematic illustration of the sputtering process employed in a sputtering chamber for deposition of  $\text{SrMoO}_3$  thin films from a  $\text{SrMoO}_4$  sintered target; (b) a photograph of the sputtering chamber during deposition with TSD of 2.5 cm.

STEM) imaging, energy dispersive X-ray spectroscopy (EDS) mapping and nano-beam electron diffraction (NBED) using a Cs-corrected FEI Titan G2 80–200 ChemiSTEM operated at 200 kV. Temperature dependence of the DC-electrical resistivity and Hall resistance from 50 K to 300 K were evaluated using the standard four-probe van der Pauw method with a physical property measurement system (VersaLab, Quantum Design, USA).

## Results and discussions

### Thin film synthesis and film surface characterizations

A systematic optimization process was employed to determine the precise synthesis parameters for SMO thin films. Firstly, clean STO(001) substrates were subjected to a pre-deposition heat treatment at  $800^\circ\text{C}$  yielding a terrace surface morphology as shown in Fig. S1 of the Supplementary Information (SI), which is a prerequisite for high quality thin films. Next, we established the Ar pressure required to obtain the desired Sr:Mo stoichiometry (= 1:1). The Sr/Mo atomic ratio in the SMO films as a function of the Ar pressure is shown in Fig. S2 of SI. We found that the Ar pressure of 10 Pa led to the desired Sr/Mo atomic ratio in the formed films. The optimum power for the least resistive SMO thin film was determined to be 100 W (see Fig S3). Further, an epitaxial growth of SMO films on STO(001) substrates could be attained only when the deposition temperature  $T_s$  was maintained at  $624^\circ\text{C}$ , in comparison to depositions made at room temperature and  $400^\circ\text{C}$ . Hence, using this Ar pressure, RF power, and  $T_s$  during deposition, epitaxial SMO with (001) orientation was grown on a STO (001) substrate pre-baked at  $800^\circ\text{C}$ .

Figures 2(a–f) represent the typical RHEED patterns observed for the SMO films deposited at

TSD = 1.0, 2.5, and 6.2 cm, respectively. The incident electron beam azimuths were parallel to the STO[100] and STO[110] directions. The RHEED patterns for other TSDs are shown in Fig. S3 of SI while that of the STO (001) substrate is also shown in Fig. S4. The narrow streaks observed in the patterns along both the azimuths clearly indicate (001) epitaxial growth of the SMO films. The longest streak patterns with the highest intensity were observed for the film deposited when TSD = 2.5 cm. Figure 3 depicts the graphical illustration of the TSD dependence of the peak-to-valley roughness ( $P-V$ , left axis) and the average surface roughness ( $R_a$ , right axis) of the films. The lowest  $P-V \sim 1.37$  nm and  $R_a \sim 0.13$  nm were achieved for TSD = 2.5 cm. The inset of Figure 3 shows 3-dimensional AFM images for TSD = 1.0 cm and 2.5 cm. We observed that the film for TSD = 1.0 cm exhibited particle agglomeration or growth of clusters which contributed to high values of  $P-V$  and  $R_a$ , while the film for TSD = 2.5 cm showed a uniform growth.

### Thin film structural characterizations

Figure 4(a) shows the out-of-plane XRD patterns of 30-nm-thick SMO films with various TSDs. We clearly observed Bragg reflections corresponding to SMO (001), SMO(002), and SMO(003) from all the films. However, except for TSD = 2.5 cm, additional peaks are observed at  $\sim 29.5^\circ$  and  $\sim 61.2^\circ$ , which are not assigned to the perovskite structure and could be attributed to the secondary phase of  $\text{SrMoO}_4$  belonging to the tetragonal  $I4_1/a$  space group. Moreover, as the TSD decreased from 15.2 cm to 6.2 cm, the peak intensity of SMO(00 $l$ ) increased while the secondary peaks gradually reduced and finally vanished at TSD  $\sim 2.5$  cm. Interestingly, when we further reduced the TSD to 1.0 cm, the secondary peak reappeared again. Thus, the TSD is the most crucial factor in

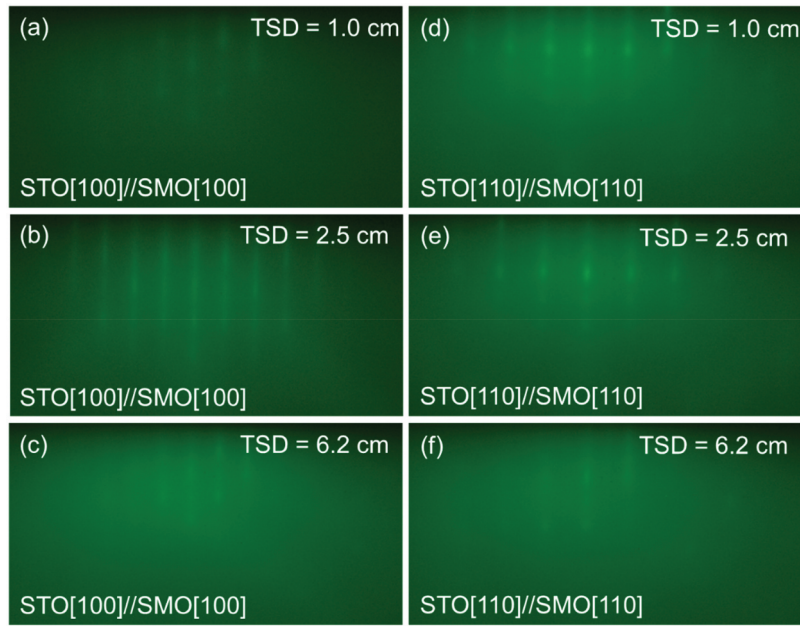


**Figure 2.** RHEED patterns for the surface of SMO (30 nm) films deposited at  $T_s = 624^\circ\text{C}$  on STO(001) substrates with the incident electron beam parallel to (a)-(c) STO[100] and (d)-(f) STO[110] azimuth, respectively. (a) and (d) TSD = 1.0 cm, (b) and (e) 2.5 cm, and (c) and (f) 6.2 cm, respectively.

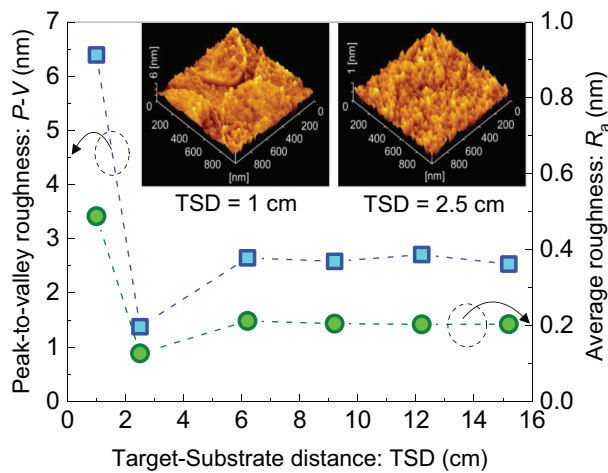


**Figure 3.** TSD dependence of  $P-V$  and  $R_a$  for SMO (30 nm) films. The inset shows AFM images for TSD = 1.0 cm and TSD = 2.5 cm.

obtaining single phase SMO films using pure Ar gas. The out-of-plane lattice parameter of the SMO film for TSD = 2.5 cm was calculated to be  $c \sim 0.404$  nm which is slightly larger ( $\sim 1.6\%$ ) than the bulk value,  $a_{\text{bulk}} = 0.3976$  nm [36]. Figure 4(b) exhibits the reciprocal space map (RSM) around the STO(204) Bragg reflection for TSD = 2.5 cm. The  $Q_{100}$  component of the SMO(204) Bragg peak is clearly observed and deviates from the peak of STO(204), indicating that the in-plane lattice parameters of the SMO film are not fully locked by the STO substrate. The estimated in-plane lattice constant of the least resistive SMO thin film was determined to be  $a \sim 0.396$  nm, slightly lower than the  $c$  value ( $\sim 0.404$  nm). Furthermore, we evaluated the XRD in-plane scan ( $\phi$ -scan) for the SMO (204) plane. Figure 4(c) represents the  $\phi$ -scan profile

of the film prepared at TSD = 2.5 cm, clearly showing the four-fold peaks expected for a cubic perovskite structure. From these results, we conclude that the single phase SMO film is epitaxially grown on a STO (001) substrate using Ar 10 Pa, TSD = 2.5 cm, and  $T_s = 624^\circ\text{C}$ .

The cross-sectional microstructures of the SMO film with TSD = 2.5 cm and  $T_s = 624^\circ\text{C}$  were characterized using STEM, as shown in Figure 5. The low magnification HAADF-STEM image in Figure 5(a) reveals very sharp and smooth interfaces at the SMO/STO substrate. The NBED patterns obtained from the SMO film and STO substrate are shown in Figure 5(b) and (c) Figures 5(b) and 5(c), respectively, with the viewing directions along SMO[100] and STO[100]. Therefore, the epitaxial relationship between SMO and STO was determined to be SMO(001)[100]//STO(001)[100]. The EDS maps in Figure 5(d) display the elemental distribution corresponding to the rectangular framed region in Figure 5(a), indicating homogeneous distribution of each element in the SMO film, and no apparent elemental interdiffusion at the interface. The corresponding EDS line profiles shown in Figure 5(e) revealed that the Mo/Sr ratio in the SMO layer is close to 1, and the O signal remains unchanged from the STO to SMO region. The atomic-resolution HAADF-STEM image in Figure 5(f) exhibits an atomically flat SMO(001)/STO(001) interface. Since the HAADF contrast of the atomic column is nearly proportional to the square of the atomic number  $Z$  of the element ( $Z$ : 22 for Ti, 38 for Sr and 42 for Mo), the Sr atomic columns have a brighter contrast than that of Ti in

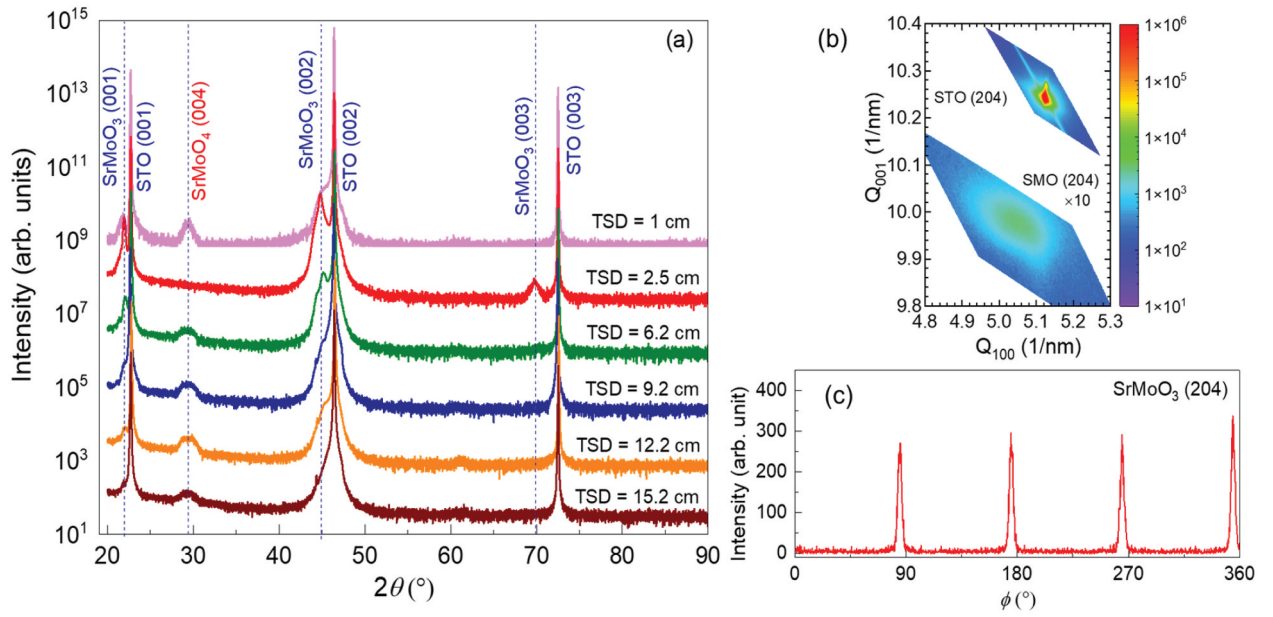


**Figure 4.** (a) Out-of-plane XRD patterns for various TSDs of SMO (30 nm) films. (b) RSM results around the STO(204) and SMO(204) reflections and (c)  $\phi$ -scan pattern of the SMO(204) lattice planes for TSD = 2.5 cm and  $T_s = 624^\circ\text{C}$ .

STO, while the light element O ( $Z: 8$ ) could not be clearly observed [37,38]. The intensity difference between Sr and Mo atomic columns in the SMO layer seems to be much smaller due to their similar atomic numbers. The schematic atomic model shown in the inset of Figure 5(f) illustrates a nearly perfect lattice matching at the SMO/STO interface. In addition, as shown in Figure 5(g), the perfect lattice matching is further confirmed by the lattice outline image, which was obtained from the inverse fast Fourier transform (IFFT) image with masking  $\{010\}$  diffractions of the FFT image of Figure 5(f) as marked by dotted circles in the inset of Figure 5(g). These microstructural analyses indicate the high quality of the SMO films obtained using RF sputtering in the pure Ar ambience with TSD = 2.5 cm. We also note that the RSM result shown in Figure 4(b) implies that the in-plane lattice parameters of the SMO film are not fully locked by the STO substrate, but HAADF-STEM images shown in Figure 5 imply lattice matching. These results indicate that the SMO film has an epitaxial strain ( $\sim 1.4\%$ ) from the substrate around the interface, and it gradually relaxes with increasing the film thickness.

### Electric transport properties

Figure 6(a) shows the TSD dependence of the RT resistivity ( $\rho_{300\text{K}}$ ) for the 30-nm-thick SMO films measured using the van der Pauw method. The SMO film for TSD = 2.5 cm exhibits the lowest  $\rho_{300\text{K}}$ . The value of  $\rho_{300\text{K}}$  significantly changes with TSD, decreasing dramatically from  $1.46 \times 10^5 \mu\Omega\text{-cm}$  for TSD = 15.2 cm to  $310 \mu\Omega\text{-cm}$  for TSD = 2.5 cm, while orders of magnitude increase to

$1.98 \times 10^6 \mu\Omega\text{-cm}$  for TSD = 1.0 cm is observed. The lowest  $\rho_{300\text{K}}$  for TSD = 2.5 cm is comparable to the reported value for a SMO film deposited using PLD [27] and is lower than the resistivity of SMO films previously grown by magnetron sputtering with hydrogen-containing plasma [25,35]. We also investigated the SMO thickness  $t_{\text{SMO}}$  dependence of  $\rho_{300\text{K}}$  in the range between 10 nm and 100 nm for TSD = 2.5 cm, as shown in Figure 6(b). The  $\rho_{300\text{K}}$  gradually decreases with increasing  $t_{\text{SMO}}$ . When  $t_{\text{SMO}} < 20$  nm, the  $\rho_{300\text{K}}$  increases rapidly, almost doubling that of 100 nm. These results attribute the SMO film conductivity to the film region rather than the SMO/STO interface [39,40].

Next, we investigated the temperature  $\rho T$  dependence of the resistivity  $\rho$  to unveil the underlying conduction mechanisms in the SMO films fabricated at different TSDs. Figure 6(c) shows the normalized plots of  $(T)/\rho_{300\text{K}}$  versus temperature for different TSDs. The film with TSD of 2.5 cm exhibits the lowest resistivity over the entire  $T$  range. The  $\rho(T)$  for films deposited when TSD = 2.5 cm and 6.2 cm increases with decrease in  $\rho T$ , exhibiting a metallic trend, similar to that of conductive SMO films deposited using PLD [24,27]. On the other hand, the films with TSD = 15.2 and 1.0 cm show a semiconductor-like behavior where  $\rho$  increases with  $T$ . We fitted the  $(T)/\rho_{300\text{K}}$  vs.  $T$  plots of TSD = 2.5, 6.2 and 15.2 cm to the power law expression given as [27],

$$\frac{\rho(T)}{\rho_{300\text{K}}} = R_0 + AT + BT^2 \quad (1)$$

where  $R_0$  is related to the residual resistivity of the films, while  $A$  and  $B$  are the coefficients of the temperature dependent terms. The  $T$  and  $T^2$  terms represent the contributions of electron-

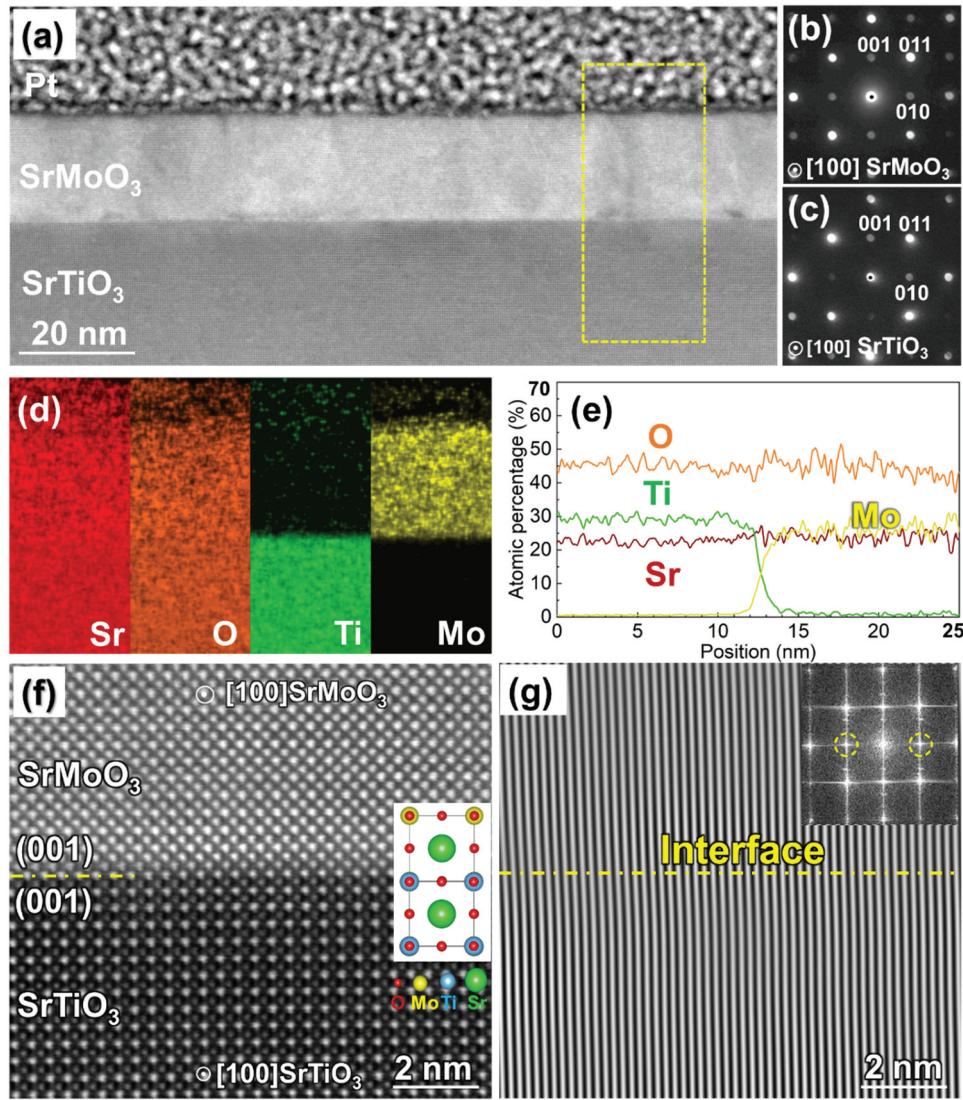


**Figure 5.** (a) Low magnification cross-sectional HAADF-STEM image of SMO film on STO(001) substrate. (b) and (c) are [001] NBED patterns acquired along SMO[100] and STO[100], respectively. (d) EDS maps collected from the region marked by a dashed-line rectangular frame in (a), and (e) corresponding EDS line profiles. (f) High magnification HAADF-STEM image near the SMO(001)/STO(001) interface. (g) IFFT filtered outline image of (f). The inset of (g) shows the FFT image of (f) and filter areas (dotted circles) for obtaining (g).

phonon and electron–electron scatterings to the resistivity, respectively [27]. The sign of  $A$  is important in determining the type of conduction; a positive sign represents the behavior of a metallic conductor, while a negative sign represents a semiconducting behavior. All the SMO films except for TSD = 1.0 cm were well fitted by Equation (1) as shown in the lower panel of Figure 6(c) and the extracted fitting parameters are listed in Table 1. For the films for TSD = 2.5 cm and 6.2 cm, the parameter  $A$  is positive, indicating that the films exhibit metallic behavior. This is attributed to the delocalized  $d$  electrons in the  $\text{Mo}^{4+}$  valence state [41–43]. In contrast,  $A$  of the film for TSD = 15.2 cm is negative, indicating a semiconductor-like behavior; this may be due to the presence of the  $\text{SrMoO}_4$  secondary phase.

Since the resistivity for TSD = 1.0 cm is much higher than that for other TSDs, we used a combined model of two-dimensional Mott variable-range hopping (VRH) [44] and electron-phonon scattering [45] to describe its conduction behavior with the following equation:

$$\begin{aligned} \rho T / \rho_{300\text{K}} &= \rho_{\text{VRH}} + \rho_{\text{SC}} \\ &= \rho_{\text{VRH0}} \exp\left(\frac{T_0}{T}\right)^{1/3} + R'_0(1 + A'(T - T_0)) \end{aligned} \quad (2)$$

where  $\rho_{\text{VRH}}$  is the mathematical form of the VRH of localized carriers and  $\rho_{\text{SC}}$  denotes the linear dependence of the resistivity on temperature due to electron-phonon scattering.  $\rho_{\text{VRH0}}$  and  $R'_0 A'$  represent the relative contributions of the two

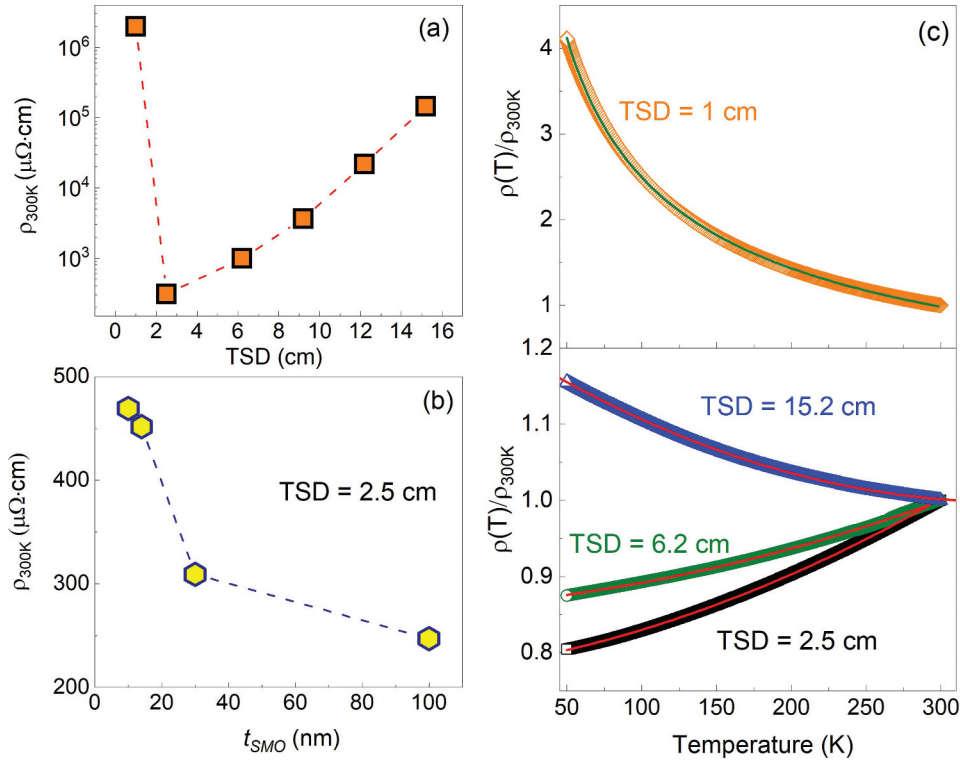


**Figure 6.** (a) TSD dependence of the resistivity at 300 K ( $\rho_{300K}$ ) of the SMO films, (b)  $\rho_{300K}$  as a function of the SMO thickness for TSD = 2.5 cm. (c) temperature dependence of the resistivity: upper panel: TSD = 1.0 cm, lower panel: 2.5 cm, 6.2 cm and 15.2 cm. The green solid line of the upper panel indicates the fitting result of Equation (2). The red solid lines of the lower panel indicate fitting results using Equation (1).

**Table 1.** The fitting parameters  $R_0$ ,  $A$ , and  $B$  obtained from fitting in Figure 6(c) using Equation (1).

TSD (cm)	$R_0$	$A$ ( $K^{-1}$ )	$B$ ( $K^{-2}$ )
2.5	0.78	$3.36 \times 10^{-4}$	$1.31 \times 10^{-6}$
6.2	0.86	$1.82 \times 10^{-4}$	$8.94 \times 10^{-7}$
15.2	1.21	-0.001	$1.80 \times 10^{-6}$

mechanisms to the resistivity, respectively.  $T_0$  is 50 K, the lowest temperature in the experiment, and  $A'$  is the temperature coefficient of the resistivity. The data for TSD = 1.0 cm were well fitted by Equation (2) as shown in the upper panel of Figure 6(c), suggesting a complex conduction mechanism for the film obtained at TSD = 1 cm. The values of fitting parameters were obtained to be  $\rho_{VRH0} = 3.2$ ,  $A' = -0.25 \times 10^{-4}$ , and  $R_0' = -4.6$ . The contribution of the Mott VRH mechanism to  $\rho T/\rho_{300K}$  is much larger ( $\sim 10^4$  order) compared to electron-phonon scattering phenomenon. In general, Mott VRH is more pronounced in disordered thin films, where localized electron motion dominates, resulting in an exponential temperature dependence of resistivity. Thus, the film deposited at TSD = 1 cm behaves as a highly disordered semiconductor system characterized by localized charge carrier states. In addition, the negative sign of  $A'$  also confirms the semiconducting nature of the film. Thus, the studies of the temperature dependence of the resistivity provide evidence for a change in the conduction mechanism with TSDs.

We further performed Hall measurements on the SMO films exhibiting a metallic behavior (TSD = 2.5 and 6.2 cm). The Hall voltages  $V_H$  of the SMO films contain only the ordinary Hall effect contribution, which can be described by the following equation [46]:

$$V_H = \frac{R_H I H}{t_{SMO}}, \quad (3)$$

where  $R_H$  is the Hall coefficient,  $I$  is the current, and  $t_{SMO}$  is the film thickness (30 nm).  $R_H$  can be extracted by calculating the slope from the study of the Hall resistance as a function of magnetic field  $H$ . The carrier concentration  $n_e$  and mobility  $\mu_e$  in the SMO film were obtained from the following relationships:  $n_e = 1/R_H e$  and  $\mu_e = 1/n_e \rho = R_H/\rho$ , where  $e$  is  $1.602 \times 10^{-19}$  C and  $\rho$  is the resistivity at a given temperature. Figure 7(a) shows the transverse Hall resistance  $R_{xy}$  of the SMO films for TSD = 2.5 and 6.2 cm, which was measured under an out-of-plane magnetic field. Considering the geometry of our Hall measurement, we conclude that electrons are the dominant charge carriers for the conductive SMO films. Figures 7(b)-(d) show the temperature dependence of  $R_H$ , electron concentration  $n_e$ , and electron mobility  $\mu_e$ , respectively. From these data, we observe that  $\mu_e$  decreases with increasing temperature, while  $R_H$  and  $n_e$  exhibit a very weak temperature dependence. The decrease in  $\mu_e$  can be understood as an increase in the amplitude of the lattice vibrations with increase in temperature, which leads to a higher susceptibility to carrier

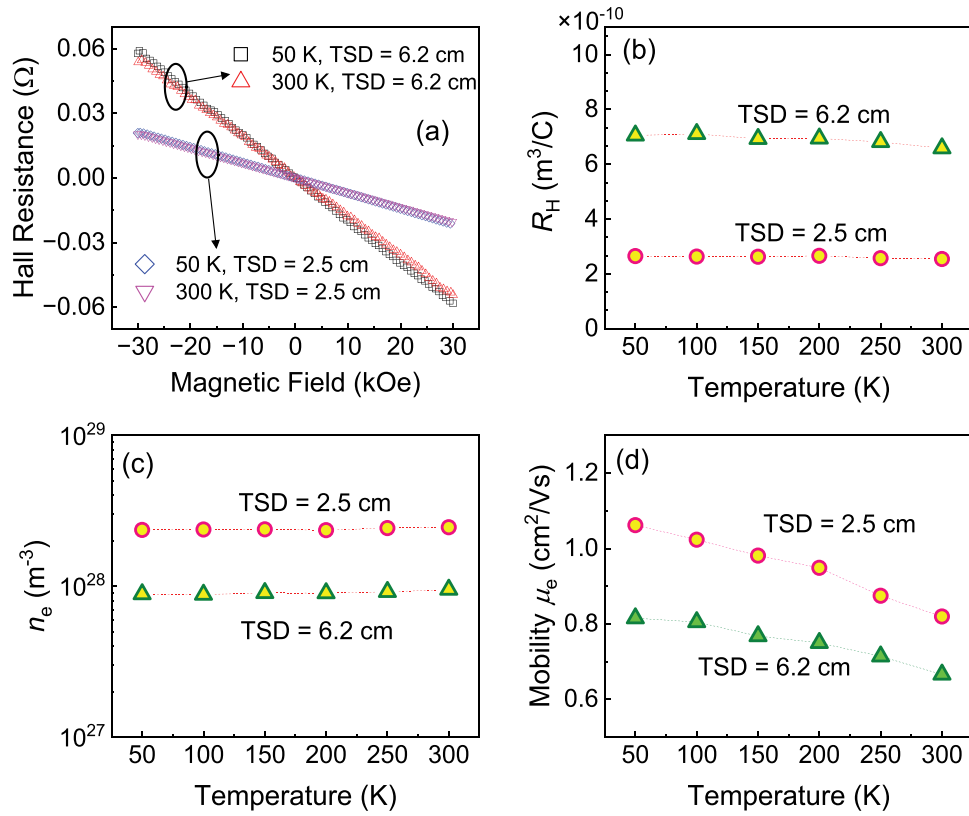


**Figure 7.** (a) Out-of-plane magnetic field dependence of hall resistance at 50 and 300 K of the films for TSD = 2.5 and 6.2 cm. Temperature-dependences of (b)  $R_H$ , (c)  $n_e$ , and (d)  $\mu_e$ .

collisions and consequently results in a decrease in  $\mu_e$ . The SMO film for TSD = 2.5 cm with the lowest resistivity exhibits a high  $n_e$  value of  $\sim 2.5 \times 10^{28} \text{ m}^{-3}$ , which is in good agreement with the theoretically calculated value of  $\sim 3.2 \times 10^{28} \text{ m}^{-3}$  for correlated  $4d^2$  SMO thin films assuming a contribution of two  $4d$  electrons per Mo to a unit cell [15]. The maximum  $\mu_e$  is  $\sim 1.1 \text{ cm}^2/\text{Vs}$ , which is also comparable to that of a PLD-deposited SMO film [15].

Finally, we discuss the formation mechanism of the conductive single-phase SMO films by modulating the TSDs. The strong TSD dependence indicates a plasma-assisted SMO formation origin. The visible plasma for the optimum TSD = 2.5 cm at 100 W surrounds a volume of  $\sim 114 \text{ cm}^3$  between a 3-inch target and the substrate. In the absence of a reducing atmosphere such as a  $\text{H}_2$  gas mixture, the thermodynamically stable  $\text{SrMoO}_4$  is converted to conductive SMO in the sputtering chamber by plasma assistance, i.e.  $2\text{SrMoO}_4 \xrightarrow{\text{Plasma}} 2\text{SrMoO}_3 + \text{O}_2$ . The efficiency of this conversion is closely related to the variation of TSD. The plasma-assisted growth associated with TSD was reported for the formation of a highly (001)-textured MgO barrier for CoFeB/MgO/CoFeB magnetic tunnel junctions [47], but the mechanism was not yet clear. Here, the combination of a high Ar gas pressure  $\sim 10 \text{ Pa}$  and RF power  $\sim 100 \text{ W}$  (power density  $\sim 2.2 \times 10^{-2} \text{ W}/\text{mm}^2$ ) could promote the ionization process of the process gas atoms:  $\text{Ar} \rightarrow \text{Ar}^+ + e^-$ . The  $\text{Ar}^+$  ions accelerate

and impinge upon the sputtering cathode, i.e. the  $\text{SrMoO}_4$  target, thus ejecting sputtered ions from it by collision. Subsequently, the ‘knocked off’ electrons from the Ar atoms participate in the following reaction inside the plasma:  $\text{Mo}^{6+} + 2e^- \rightarrow \text{Mo}^{4+}$ . The conversion efficiency from  $\text{Mo}^{6+}$  to  $\text{Mo}^{4+}$  seems to increase progressively with decreasing TSD up to the optimum TSD value of 2.5 cm, as we demonstrated the change in intensity of the  $\text{SrMoO}_4(004)$  impurity peak in the XRD pattern (see Figure 4(a)) with varying TSD. The conversion efficiency reaches a maximum for TSD = 2.5 cm where no secondary phase is observed in the SMO film. A further decrease in TSD (1.0 cm) results in the reappearance of the  $\text{SrMoO}_4$  impurity peak, which may be due to (i) an increase of plasma damage into the film and (ii) a greatly enhanced sputtering rate (see Fig. S6) which results in a much shorter approach time from target to substrate compared to the plasma-assisted reduction reaction time.

### Summary

Conductive epitaxial SMO thin films with a perovskite structure were successfully synthesized by using TSD controlled RF magnetron sputtering in a pure Ar atmosphere on STO substrates via plasma assistance. A small TSD of 2.5 cm resulted in a 30 nm thick film with a flat surface, small lattice mismatch with the



substrate, no secondary phase formation, and a low resistivity of  $310 \mu\Omega\text{-cm}$  at RT. A series of TSD-dependent reactions in the plasma involving the target material and Ar gas assisted the prescribed strategy for sputter deposition in the absence of  $\text{H}_2$  in the process gas mixture, thus yielding pure phase epitaxial conductive films. Temperature dependence of the resistivity and Hall resistance shed light on the conduction mechanism of the SMO films deposited using different TSDs. For the lowest (1.0 cm) and highest TSD (15.2 cm), the prepared films exhibited semiconducting properties, while the SMO films deposited for TSD = 6.2 cm and 2.5 cm, the temperature dependence of the resistivity and Hall resistance revealed metallic behavior. SMO thin films hold promising future prospects due to their metallic conduction property and high carrier concentration which have garnered widespread interest in this material for applications in transparent conductive oxides, solid-state batteries, and photocatalysis. Additionally, ongoing research aims to explore the use of SMO in perovskite solar cells and oxide-based electronics. Therefore, achieving high-quality thin films with high RT conductivity through a  $\text{H}_2$ -free sputtering technique is critical in enhancing the potential of SMO for next-generation electronic devices.

## Disclosure Statement

No potential conflict of interest was reported by the author(s).

## Funding

This work was supported by the JST CREST under Grant No. JPMJCR19J4 and Prime Minister's Research Fellowship under May 2021 scheme (PMRF ID: 1901274) by Ministry of Education (MoE), Govt. of India. The authors thank T. Hiroto for his technical support in thin-film XRD measurements, H. Ikeda for her technical support in microfabrication of films, and S. Ghosh for useful discussions. MRC acknowledges National Institute for Materials Science, Japan availing the NIMS Internship. MRC and ST acknowledge the Indian Institute of Technology Guwahati for partial support for this work.

## ORCID

Mouli Roy-Chowdhury  <http://orcid.org/0000-0001-9128-5563>  
Zhenchao Wen  <http://orcid.org/0000-0001-7496-1339>

## References

[1] Lechermann F. Late transition metal oxides with infinite-layer structure: nickelates versus cuprates. *Phys Rev B*. 2020;101(8):081110. doi: 10.1103/PhysRevB.101.081110

- [2] Rao CNR, Cheetham AK. Giant magnetoresistance in transition metal oxides. *Science*. 1996;272(5260):369–370. doi: 10.1126/science.272.5260.369
- [3] Chen Z, Liu Z, Sun Y, et al. Two-dimensional superconductivity at the  $\text{LaAlO}_3/\text{KTaO}_3$  (110) heterointerface. *Phys Rev Lett*. 2021;126(2):026802. doi: 10.1103/PhysRevLett.126.026802
- [4] Moon SJ, Jin H, Kim KW, et al. Dimensionality-controlled insulator-metal transition and correlated metallic state in 5 d transition metal oxides  $\text{Sr}_{n+1}\text{Ir}_n\text{O}_{3n+1}$  ( $n=1, 2$ , and  $\infty$ ). *Phys Rev Lett*. 2008;101(22):226402. doi: 10.1103/PhysRevLett.101.226402
- [5] Tokura Y, Nagaosa N. Orbital physics in transition-metal oxides. *Science*. 2000;288(5465):462–468. doi: 10.1126/science.288.5465.462
- [6] Biswas A, Jeong YH. Effects of substrate temperature on the unusual non-fermi liquid metal to insulator transition in perovskite  $\text{SrIrO}_3$  thin films. *J Phys D Appl Phys*. 2015;48(13):135303. doi: 10.1088/0022-3727/48/13/135303
- [7] Mackenzie AP, Julian SR, Diver AJ, et al. Quantum oscillations in the layered perovskite superconductor  $\text{Sr}_2\text{RuO}_4$ . *Phys Rev Lett*. 1996;76(20):3786. doi: 10.1103/PhysRevLett.76.3786
- [8] Wang S, Liu B, Zhu Y, et al. Enhanced performance of  $\text{TiO}_2$ -based perovskite solar cells with Ru-doped  $\text{TiO}_2$  electron transport layer. *Sol Energy*. 2018;169:335–342. doi: 10.1016/j.solener.2018.05.005
- [9] Qin M, Xiao Y, Yang H, et al. Ru/Nb co-doped perovskite anode: achieving good coking resistance in hydrocarbon fuels via core-shell nanocatalysts exsolution. *Appl Catal B: Environ*. 2021;299:120613. doi: 10.1016/j.apcatb.2021.120613
- [10] Diaz-Morales O, Raaijman S, Kortlever R, et al. Iridium-based double perovskites for efficient water oxidation in acid media. *Nat Commun*. 2016;7(1):12363. doi: 10.1038/ncomms12363
- [11] Shitade A, Katsura H, Kuneš J, et al. Quantum spin hall effect in a transition metal oxide  $\text{Na}_2\text{IrO}_3$ . *Phys Rev Lett*. 2009;102(25):256403. doi: 10.1103/PhysRevLett.102.256403
- [12] Zaanen J, Sawatzky GA, Allen JW. Band gaps and electronic structure of transition-metal compounds. *Phys Rev Lett*. 1985;55(4):418. doi: 10.1103/PhysRevLett.55.418
- [13] Corredor LT, Aslan-Cansever G, Sturza M, et al. Iridium double perovskite  $\text{Sr}_2\text{YIrO}_6$ : a combined structural and specific heat study. *Phys Rev B*. 2017;95(6):064418. doi: 10.1103/PhysRevB.95.064418
- [14] Lee YS, Lee JS, Noh TW, et al. Systematic trends in the electronic structure parameters of the 4d transition-metal oxides  $\text{SrMO}_3$  ( $M= \text{Zr}, \text{Mo}, \text{Ru}$ , and  $\text{Rh}$ ). *Phys Rev B*. 2003;67(11):113101. doi: 10.1103/PhysRevB.67.113101
- [15] Ha Y, Lee S. Oxygen-Vacancy-endurable conductors with enhanced transparency using correlated 4d<sup>2</sup>  $\text{SrMoO}_3$  thin films. *Adv Funct Mater*. 2020;30(28):2001489. doi: 10.1002/adfm.202001489
- [16] Stoner JL, Murgatroyd PA, O'Sullivan M, et al. Chemical control of correlated metals as transparent conductors. *Adv Funct Mater*. 2009;29(11):1808609. doi: 10.1002/adfm.201808609
- [17] Salg P, Walk D, Zeinar L, et al. Atomically interface engineered micrometer-thick  $\text{SrMoO}_3$  oxide electrodes for thin-film  $\text{Ba}_x\text{Sr}_{1-x}\text{TiO}_3$  ferroelectric varactors

- tunable at low voltages. *APL Mater.* 2019;7(5). doi: [10.1063/1.5094855](https://doi.org/10.1063/1.5094855)
- [18] Onos Y, Tokura Y. Doping dependence of the anomalous hall effect in  $\text{La}_{1-x}\text{Sr}_x\text{CoO}_3$ . *Phys Rev B.* 2006;73(17):174421. doi: [10.1103/PhysRevB.73.174421](https://doi.org/10.1103/PhysRevB.73.174421)
- [19] Jadaun P, Register LF, Banerjee SK. Rational design principles for giant spin hall effect in 5d-transition metal oxides. *Proc Natl Acad Sci USA.* 2020;117(22):11878–11886. doi: [10.1073/pnas.1922556117](https://doi.org/10.1073/pnas.1922556117)
- [20] Medvedeva JE. Magnetically mediated transparent conductors:  $\text{In}_2\text{O}_3$  doped with Mo. *Phys Rev Lett.* 2006;97(8):086401. doi: [10.1103/PhysRevLett.97.086401](https://doi.org/10.1103/PhysRevLett.97.086401)
- [21] Egbo KO, Adesina AE, Ezech CV, et al. Effects of free carriers on the optical properties of high mobility transition metal doped  $\text{In}_2\text{O}_3$  transparent conductors. *Phys Rev Mater.* 2021;5(9):094603. doi: [10.1103/PhysRevMaterials.5.094603](https://doi.org/10.1103/PhysRevMaterials.5.094603)
- [22] Magyari-Köpe B, Tendulkar M, Park SG, et al. Resistive switching mechanisms in random access memory devices incorporating transition metal oxides:  $\text{TiO}_2$ ,  $\text{NiO}$  and  $\text{Pr}_{0.7}\text{Ca}_{0.3}\text{MnO}_3$ . *Nanotechnology.* 2011;22(25):254029. doi: [10.1088/0957-4484/22/25/254029](https://doi.org/10.1088/0957-4484/22/25/254029)
- [23] Nagai I, Shirakawa N, Ikeda SI, et al. Highest conductivity oxide  $\text{SrMoO}_3$  grown by a floating-zone method under ultralow oxygen partial pressure. *Appl Phys Lett.* 2005;87(2):024105. doi: [10.1063/1.1992671](https://doi.org/10.1063/1.1992671)
- [24] Wang HH, Cui DF, Zhou YL, et al. Growth and characterization of  $\text{SrMoO}_3$  thin films. *J Cryst Growth.* 2001;226(2–3):261–266. doi: [10.1016/S0022-0248\(01\)00799-0](https://doi.org/10.1016/S0022-0248(01)00799-0)
- [25] Mizoguchi H, Kitamura N, Fukumi K, et al. Optical properties of  $\text{SrMoO}_3$  thin film. *J Appl Phys.* 2000;87(9):4617–4619. doi: [10.1063/1.373111](https://doi.org/10.1063/1.373111)
- [26] Zhu M, Li P, Hu L, et al. Thickness dependence of metal–insulator transition in  $\text{SrMoO}_3$  thin films. *J Appl Phys.* 2022;132(7):075303. doi: [10.1063/5.0098993](https://doi.org/10.1063/5.0098993)
- [27] Lekshmi IC, Gayen A, Hegde MS. The effect of strain on nonlinear temperature dependence of resistivity in  $\text{SrMoO}_3$  and  $\text{SrMoO}_{3-x}\text{N}_x$  films. *Mater Res Bull.* 2005;40(1):93–104. doi: [10.1016/j.materresbull.2004.09.004](https://doi.org/10.1016/j.materresbull.2004.09.004)
- [28] Salg P, Zeinar L, Radetinac A, et al. Oxygen diffusion barriers for epitaxial thin-film heterostructures with highly conducting  $\text{SrMoO}_3$  electrodes. *J Appl Phys.* 2020;127(6):065302. doi: [10.1063/1.5129767](https://doi.org/10.1063/1.5129767)
- [29] Radetinac A, Mani A, Melnyk S, et al. Highly conducting  $\text{SrMoO}_3$  thin films for microwave applications. *Appl Phys Lett.* 2014;105(11):114108. doi: [10.1063/1.4896339](https://doi.org/10.1063/1.4896339)
- [30] Wang HH, Yang GZ, Cui DF, et al. Epitaxial growth and electric characteristics of  $\text{SrMoO}_3$  thin films. *J Vac Sci Technol A: Vac Surf Films.* 2001;19(3):930–933. doi: [10.1116/1.1355756](https://doi.org/10.1116/1.1355756)
- [31] Lung C, Toma M, Pop M, et al. Characterization of the structural and optical properties of  $\text{ZnO}$  thin films doped with Ga, Al and (Al + Ga). *J Alloys Compd.* 2017;725:1238–1243. doi: [10.1016/j.jallcom.2017.07.265](https://doi.org/10.1016/j.jallcom.2017.07.265)
- [32] Lee J, Lee D, Lim D, et al. Structural, electrical and optical properties of  $\text{ZnO}$ : Al films deposited on flexible organic substrates for solar cell applications. *Thin Solid Films.* 2007;515(15):6094–6098. doi: [10.1016/j.tsf.2006.12.099](https://doi.org/10.1016/j.tsf.2006.12.099)
- [33] Toma M, Marconi D, Pop M, et al. Influence of substrate-target distance on structural and optical properties of Ga and (Al+ Ga)-doped  $\text{ZnO}$  thin films deposited by radio frequency sputtering. *Analytical Lett.* 2019;52(14):2227–2238. doi: [10.1080/00032719.2019.1606819](https://doi.org/10.1080/00032719.2019.1606819)
- [34] Inukai T, Murakami T. Preparation of conductive  $\text{SrMoO}_3$  thin films and their application to electrodes for thin film capacitors. *Jpn J Appl Phys.* 1985;24(S3):21. doi: [10.7567/JJAPS.24S3.21](https://doi.org/10.7567/JJAPS.24S3.21)
- [35] Ryu HU, Sun HJ. Preparation of conductive  $\text{SrMoO}_3$  thin films by RF magnetron sputtering and evaluation of their electrical conduction properties. *J Korean Inst Electr Electron Mater Eng.* 2011;24(6):468–472. doi: [10.4313/JKEM.2011.24.6.468](https://doi.org/10.4313/JKEM.2011.24.6.468)
- [36] Macquart RB, Kennedy BJ, Avdeev M. Neutron diffraction study of phase transitions in perovskite-type strontium molybdate  $\text{SrMoO}_3$ . *J Solid State Chem.* 2010;183(1):250–255. doi: [10.1016/j.jssc.2009.11.005](https://doi.org/10.1016/j.jssc.2009.11.005)
- [37] Hartel P, Rose H, Dinges C. Conditions and reasons for incoherent imaging in STEM. *Ultramicroscopy.* 1996;63(2):93–114. doi: [10.1016/0304-3991\(96\)00020-4](https://doi.org/10.1016/0304-3991(96)00020-4)
- [38] He C, Li Z, Chen H, et al. Unusual solute segregation phenomenon in coherent twin boundaries. *Nat Commun.* 2021;12(1):722. doi: [10.1038/s41467-021-21104-8](https://doi.org/10.1038/s41467-021-21104-8)
- [39] Namba Y. Resistivity and temperature coefficient of thin metal films with rough surface. *Jpn J Appl Phys.* 1970;9(11):1326. doi: [10.1143/JJAP.9.1326](https://doi.org/10.1143/JJAP.9.1326)
- [40] Barua S, Rajeev KP. Status of surface conduction in topological insulators. *AIP Adv.* 2014;4(1). doi: [10.1063/1.4864058](https://doi.org/10.1063/1.4864058)
- [41] Mizoguchi H, Fukumi K, Kitamura N, et al. Electronic structure of polycrystalline  $\text{AMoO}_3$  (A= Sr or Ba). *J Appl Phys.* 1999;85(9):6502–6505. doi: [10.1063/1.370288](https://doi.org/10.1063/1.370288)
- [42] Wells MP, Zou B, Doiron BG, et al. Tunable, low optical loss strontium molybdate thin films for plasmonic applications. *Adv Opt Mater.* 2017;5(22):1700622. doi: [10.1002/adom.201700622](https://doi.org/10.1002/adom.201700622)
- [43] Hopper HA, Le J, Cheng J, et al. An investigation of the optical properties and water splitting potential of the coloured metallic perovskites  $\text{Sr}_{1-x}\text{Ba}_x\text{MoO}_3$ . *J Solid State Chem.* 2016;234:87–92. doi: [10.1016/j.jssc.2015.12.002](https://doi.org/10.1016/j.jssc.2015.12.002)
- [44] Gantmakher VF. *Electrons and disorder in solids.* Vol. 130. (NY) (NY): Oxford University Press; 2005.
- [45] Russo U, Ielmini D, Cagli C, et al. Filament conduction and reset mechanism in  $\text{NiO}$ -based resistive-switching memory (RRAM) devices. *IEEE Trans Electron Devices.* 2009;56(2):186–192. doi: [10.1109/TED.2008.2010583](https://doi.org/10.1109/TED.2008.2010583)
- [46] Hall EH. On a new action of the magnet on electric currents. *Am J Sci.* 1880;3(111):200–205. doi: [10.2475/ajs.s3-19.111.200](https://doi.org/10.2475/ajs.s3-19.111.200)
- [47] Choi GM, Shin KH, Seo SA, et al. Substrate biasing effect during  $\text{MgO}$  deposition in  $\text{CoFeB}/\text{MgO}/\text{CoFeB}$  MTJs. *IEEE Trans Magn.* 2009;45(6):2371–2373. doi: [10.1109/TMAG.2009.2018577](https://doi.org/10.1109/TMAG.2009.2018577)